Multiphoton Near-Infrared Quantum Splitting of Er^{3+}

Dechao Yu,[1,2] Ting Yu[1,2] Yingzhi Wang,[1] Qinyuan Zhang,[1,*] and Andries Meijerink[2,†]

[1]*State Key Laboratory of Luminescent Materials and Devices, and Institute of Optical Communication Materials, South China University of Technology, Guangzhou 510641, P. R. China*

[2]*Debye Institute for Nanomaterials Science, Utrecht University, 3508 TA Utrecht, Netherlands*

The efficiency of single-junction solar cells is limited to about 30% (the Shockley-Queisser limit). Spectral mismatch losses (transparency to low-energy photons, thermalization of high-energy photons) strongly contribute to lowering the maximum efficiency. To reduce thermalization losses, photon splitting is proposed and observed for a variety of lanthanide-doped materials. For Er^{3+}, even a one-to-three photon-splitting process has been reported, yielding three IR photons at around 1530 nm following absorption of one blue-green photon. This is especially beneficial for narrow band gap solar cells, such as crystalline Ge. Here, we report on photon splitting for Er^{3+} in YVO$_4$. Following absorption in the ^{2}H$_{11/2}$ and ^{4}S$_{3/2}$ levels (520–550 nm), efficient cross-relaxation (CR) yields two excited Er^{3+} ions: one in the ^{4}I$_{9/2}$ state and one in the ^{4}I$_{13/2}$ state (CR1). A second CR step from the ^{4}I$_{9/2}$ state, leaving both Er^{3+} ions in the ^{4}I$_{13/2}$ excited state (CR2), is crucial in realizing efficient three IR photon splitting. It is demonstrated here that the second step has a low efficiency, as a result of competing fast multiphonon relaxation, ^{4}I$_{9/2} \rightarrow {}^4$I$_{11/2}$, and a large energy mismatch, which makes the CR2 step thermally activated. Based on experiments and theory, a maximum quantum efficiency of 170% is calculated for IR emission, following blue-green excitation in YVO$_4$:Er^{3+}. An outlook is presented for three-photon splitting in low-phonon-energy hosts, where nonradiative multiphonon relaxation is suppressed. The anti-Stokes nature of the second CR step makes three-photon splitting unlikely and prevents the realization of IR quantum yields above 200%.

I. INTRODUCTION

Conversion of the energy of solar photons into electricity using solar cells is one of the most important options to generate green and renewable energy because it is capable of supplying sufficient energy to meet the long-term worldwide energy demand. However, even for a state-of-the-art single-junction crystalline Si (*c*-Si) solar cell, the energy efficiency is only about 15%–20%, and the theoretical maximum efficiency, known as the Shockley-Queisser efficiency limit, is about 30%, which is far below unity [1,2]. The most significant contribution to the efficiency loss in solar cells is related to so-called spectral mismatch losses. In a single-junction solar cell, only one electron-hole pair is created per absorbed photon, with an energy equal to or higher than the band gap, E_g, of the semiconductor material, irrespective of the photon energy. Excess energy is dissipated as heat as the "hot" charge carriers relax to the band edges. This is known as thermalization

losses. Photons with energies lower than E_g cannot be absorbed and are transmitted (giving rise to transmission losses). For *c*-Si with a band gap of 1.12 eV (corresponding to approximately 1100 nm photons), thermalization losses are significant and these losses increase for narrower band-gap solar cells, such as *c*-Ge, with a band gap of 0.67 eV (~1850 nm) [3,4]. To reduce thermalization losses, a promising approach is to split one incident ultraviolet-to-visible (UV-vis) photon into multiple near-infrared (NIR) photons, which can be absorbed by solar cells to generate multiple electron-hole pairs for each high-energy photon [3,5–7]. This process is known as quantum splitting (QS) or down-conversion and can greatly improve the conversion efficiency of solar cells, especially those with narrow band gaps, where thermalization losses are the major loss factor [6,7]. Trupke *et al.* estimated that a combination of an ideal down-conversion layer with a single-junction *c*-Si cell increased its theoretical efficiency from about 30% to 40% [7]. Similar calculations reveal that, for a solar cell with a smaller band gap (E_g of 0.8 eV), 20% efficiency can be gained through a one-to-two down-conversion (see green area in Fig. S1 within the Supplemental Material [8]), and a one-to-three down-conversion for the higher

———————
*qyzhang@scut.edu.cn
†a.meijerink@uu.nl

energy photons allows an increase of an additional 5% (see blue area in Fig. S1 within the Supplemental Material [8]).

Quantum splitting is a linear process and even for low excitation densities it is possible to obtain high conversion efficiencies (contrary to up-conversion, which requires high excitation densities). This allows the use of nonconcentrated sunlight. In the past decade, a variety of NIR QS materials have been reported, especially RE^{3+}-Yb^{3+} (RE = Tb, Tm, Pr, Er, Nd, Ho) couples [9–19]. An absorbed UV-vis photon is cut to two NIR photons by two-step energy transfer from the RE ion to two Yb^{3+} ions, which emit at around 1000 nm, just above the E_g value of *c*-Si. More recently, several three-photon NIR QS materials for emission at 1530 nm were reported based on Er^{3+}. A triple-splitting scheme for green photons at around 520 nm is based on two consecutive cross-relaxation (partial energy transfer) steps between neighboring Er^{3+} ions [3,20–22]. After an initial cross-relaxation of $^2H_{11/2}, ^4S_{3/2} + ^4I_{15/2} \rightarrow ^4I_{9/2} + ^4I_{13/2}$ (CR1), a second cross-relaxation step of $^4I_{9/2} + ^4I_{15/2} \rightarrow ^4I_{13/2} + ^4I_{13/2}$ (CR2) results in three Er^{3+} ions in the $^4I_{13/2}$ excited state that can efficiently radiate 1530 nm photons upon returning to the $^4I_{15/2}$ ground state. The efficiency of the CR processes is, as for all energy-transfer processes, determined by several factors: (i) coupling strength for energy transfer, which increases for smaller distances between donor and acceptor; (ii) similar energy gaps (ΔE) to provide resonance for the energy-transfer steps; and (iii) stable intermediate energy levels separated by ΔE to slow down competing radiative and nonradiative decay processes [23–25]. For Er^{3+}, the ΔE values of $^2H_{11/2}, ^4S_{3/2} \rightarrow ^4I_{9/2}$, $^4I_{9/2} \rightarrow ^4I_{13/2}$, and $^4I_{13/2} \rightarrow ^4I_{15/2}$, are about 6630, 5900, and 6600 cm^{-1} [3,23,24], respectively. While the CR1 step is almost resonant (starting from the $^2H_{11/2}$ level), the CR2 process belongs to an anti-Stokes energy-transfer process, which will strongly reduce its efficiency, even at high Er^{3+} concentration. In addition, emission from the $^4I_{9/2}$ state is weak, which reveals that the intermediate $^4I_{9/2}$ state is not stable [23], especially for Er^{3+} doped into hosts with high phonon energies. The energy gap to the next lower level, $^4I_{11/2}$, is only about 2200 cm^{-1}, which can be bridged by fast multiphonon relaxation in hosts with phonon energies higher than 450 cm^{-1}. Hence, three-photon NIR QS, as reported for Er^{3+}, is not expected and the intense Er^{3+} emission at about 1530 nm might not originate from the proposed triply splitting process.

Here, we systematically study NIR photoluminescence (PL) of Er^{3+}-doped YVO_4 polycrystalline phosphors by means of diffuse reflectance spectra, photoemission, excitation, and time-resolved spectra. YVO_4 is chosen as a host because vanadate has a medium maximum phonon energy ($\hbar\omega \sim 850$–900 cm^{-1}), $Y_{1-x}Er_xVO_4$ is a perfect solid solution and vanadates are one of the hosts for which three-photon splitting with Er^{3+} is reported. Also, other studies in which three-photon emission was described

involved host lattices with similar phonon energies (i.e., silicates and aluminates). To provide insight into the photon-splitting efficiency and energy-transfer dynamics, emission and excitation spectra, as well as luminescence decay curves, are recorded as a function of Er^{3+} concentration. The results reveal that, in host lattices with phonon energies above 600 cm^{-1} (such as vanadates, silicates, and aluminates), the CR2 step is very inefficient, as a result of fast multiphonon relaxation from the $^4I_{9/2}$ to the $^4I_{11/2}$ level. Even when multiphonon relaxation is prevented in extremely low-phonon hosts, such as chalcogenide glasses, the energy mismatch and thermal activation energy for the CR2 step of about 700–800 cm^{-1} make this step inefficient, which renders the development of an efficient Er^{3+}-based three-photon splitting material cumbersome.

II. METHODS

A. Synthesis

Microcrystalline YVO_4:$x\%Er^{3+}$ ($x = 0.25, 0.5, 1, 2, 3, 5, 10, 20$) phosphors are synthesized via a conventional high-temperature solid-state reaction method. In all cases, the percentages given for Er^{3+} dopant is in mol % with respect to Y^{3+} in YVO_4 host. Starting materials of Y_2O_3 and Er_2O_3 (purity at least 4 N), and NH_4VO_3 (analytical reagent) are mixed thoroughly with the specified stoichiometric ratios by grinding in an agate mortar and pestle. The resulting homogeneous mixtures are calcined at 1100 °C in ambient atmosphere for 6 h with several intermediate grinding steps.

B. Measurements

Phase identification of all prepared products is performed on an x-ray powder diffractometer (XRD; Philips Model PW1830) using Cu $K\alpha$ ($\lambda = 1.54056$ Å) radiation at 40 and 40 mA. XRD patterns of the sample are collected over 2θ values ranging from 10° to 80° at an interval of 0.033°. Diffuse reflectance spectra of the phosphors are measured with a Cary 5000 UV-vis-NIR spectrophotometer using $BaSO_4$ as reference. The size and morphology of the as-obtained YVO_4:Er^{3+} phosphors are visualized by means of a field-emission scanning electron microscope (FE SEM; JEOL JEM-1010) using an accelerating voltage of 10.0 kV and a magnification of 15 000. Steady-state emission and excitation spectra are recorded using a FLS920 spectrophotofluorometer (Edinburgh Instruments) equipped with a 450 W xenon lamp source, TMS300 monochromators, a thermoelectronically cooled R928 photomultiplier tube (PMT), a liquid nitrogen cooled R5509-72 NIR PMT for NIR wavelengths beyond 800 nm, and by using the single-photon counting technique. Time-resolved spectra (luminescence decay curves) are measured by time-correlated single-photon counting on the FLS920 system using a pulsed excitation source,

a tunable midband pulsed OPO laser (410-2200, 20 Hz, pulsed width ∼7 ns, Opolette HE 355II). To allow for comparison of emission intensities, measurement series are performed under identical measuring conditions (sample alignment, slit widths etc.).

III. RESULTS AND DISCUSSION

A. Characterization

Crystalline YVO$_4$ has a tetragonal structure with space grou D_{4h}^{19} ($I4_1/amd$) and is composed of YO$_8$ dodecahedra (Y^{3+} point symmetry is D_{2d}) and VO$_4$ tetrahedra [symmetry D_{2d}; see the inset of Fig. 1(a)], where lanthanide dopants typically occupy Y^{3+} sites [24]. Due to similar chemical properties and effective ionic radii of Y^{3+} and Er^{3+} ($r_{Y^{3+}} = 1.02$ Å, $r_{Er^{3+}} = 1.00$ Å) [26], Y$_{1-x}$Er$_x$VO$_4$ is a perfect material to continuously vary the Er^{3+} concentration from a regime where it acts as a dopant to a regime where it serves as the main constituent [see comparison in Fig. 1(a) and similar phenomena in Ref. [23]]. In this way, we can adjust the average interionic distance of Er^3-Er^{3+} pairs and maximize the interaction between Er^{3+} ions, leading to higher CR energy-transfer rates. All measured diffraction peaks of as-prepared YVO$_4$:Er^{3+} phosphors can be well indexed to the zircon-type structure of the pure YVO$_4$ phase (JCPDS #17-0341), shown in Fig. 1(a) for comparison. No trace peaks for Er-containing or other impurity phases can be observed. These results reveal that the Er^{3+} dopants are well dissolved in the YVO$_4$ host lattice by substituting on the Y^{3+} sites.
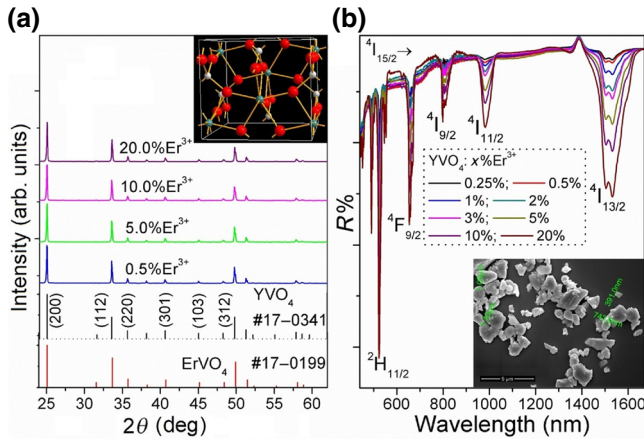
To further monitor the incorporation of Er^{3+} into YVO$_4$ host lattice, diffuse reflectance spectra are recorded. As shown in Fig. 1(b), the absorption strength of peaks corresponding to typical electronic transitions of Er^{3+} (e.g., ∼1520 nm from $^4I_{15/2} \rightarrow {}^4I_{13/2}$, ∼980 nm from $^4I_{15/2} \rightarrow {}^4I_{11/2}$) varies in good accordance with the Er^{3+} concentration present in the starting mixture. This result indicates that the Er^{3+} ions are incorporated into YVO$_4$ lattice equally well for all samples and allows for spectral comparison and analysis related to Er^{3+}-doping concentrations in different samples. Moreover, the SEM image in the inset of Fig. 1(b) indicates that YVO$_4$:Er^{3+} phosphor particles sintered at 1100 °C for 6 h have good crystallinity, while the morphology and size are irregular, with an average size around 1 μm.

B. Photoluminescence

To investigate the photon-splitting processes in YVO$_4$: Er^{3+}, first luminescence spectra are recorded in the vis and NIR spectral regions for samples doped with different Er^{3+} concentrations and treated at different temperatures. In Fig. 2, emission spectra of YVO$_4$:Er^{3+} (0.5, 1, and 2%) phosphors excited by photons of about 522 nm are shown. Apart from emission lines in the visible region around 553 and 668 nm (assigned to transitions from the $^4S_{3/2}$ and $^4F_{9/2}$ states to the $^4I_{15/2}$ state), several NIR emission bands are detected at about 856, 1000, 1236, and 1530 nm [Fig. 2(a)]. The 1530 nm emission originating from the $^4I_{13/2} \rightarrow {}^4I_{15/2}$ transition is the most intense. For clarity, the emission intensities of the lines around

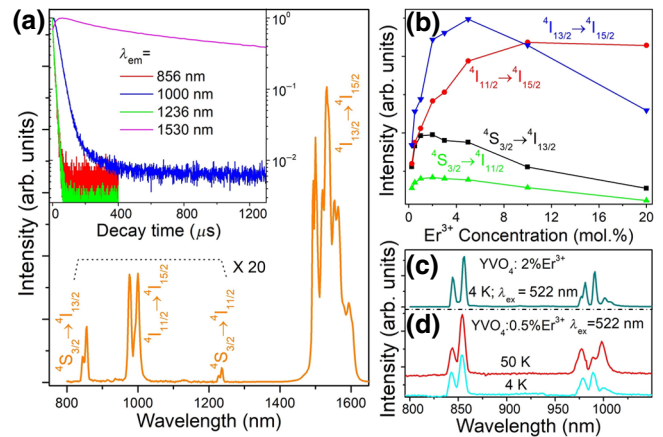FIG. 1. (a) X-ray diffraction patterns of YVO$_4$:x%Er^{3+} ($x = 0.5, 5, 10, 20$) materials synthesized and, for comparison, reference patterns of YVO$_4$ (JCPDS #17-0341) and ErVO$_4$ (JCPDS #17-0199) standards. (b) Diffuse reflectance spectra of YVO$_4$:x%Er^{3+} ($x = 0.25, 0.5, 1, 2, 3, 5, 10, 20$) phosphors. The inset of (a) shows the crystal structure of YVO$_4$ (white, gray, and red spheres represent Y^{3+}, V^{5+}, and O^{2-}, respectively). The inset in (b) shows a SEM image of as-obtained YVO$_4$:Er^{3+} microcrystals.

FIG. 2. (a) NIR emission spectra of YVO$_4$:Er^{3+} under excitation of 522 nm (note the scaling factor of 20 between the 1500 and 800–1300 nm emissions). The inset shows the decay curves of 856, 1000, 1236, and 1530 nm emissions of YVO$_4$:1%Er^{3+}. (b) Integrated intensities of NIR emissions at about 856, 1000, 1236, and 1530 nm as a function of Er^{3+} concentration in YVO$_4$. Low-temperature NIR emission spectra of YVO$_4$:2%Er^{3+} [(c); 4 K] and that of YVO$_4$:0.5%Er^{3+} [(d); 4 and 50 K] under excitation at 522 nm.

856, 1000, and 1236 nm are all enlarged 20-fold relative to that of 1530 nm. In some previous reports, it was indicated that the emissions around 856 and 1000 nm of Er^{3+} originated from the transitions of $^4I_{9/2} \rightarrow {}^4I_{15/2}$ and $^4S_{3/2} \rightarrow {}^4I_{11/2}$ [25,27], respectively. Indeed, some transitions on Er^{3+} originating from different starting levels are resonant and identification can be done by measuring luminescence lifetimes of different emission lines and by recording excitation spectra. Emissions originating from the same starting level have the same luminescence lifetime. Based on the luminescence decay curves in the inset of Fig. 2(a), as well as a comparison of emission spectra [see Fig. S2(a) within the Supplemental Material [8]] and excitation spectra [see Fig. S2(b) within the Supplemental Material [8]], we can assign 856 and 1236 nm emissions of Er^{3+}. Both originate from the same excited $^4S_{3/2}$ state (with a lifetime around several μs). This differs from the 1000 nm emission, which originates from the excited $^4I_{11/2}$ state and has a longer lifetime of around 26 μs [22].

Figure 2(b) shows the dependence of the integrated NIR emission intensities on Er^{3+} concentration. It is interesting to see that, with increasing Er^{3+} concentration, the emissions at 856 and 1236 nm increase to reach a maximum at 2%Er^{3+}, while those of 1000 and 1530 nm reach a maximum at higher concentrations (20%Er^{3+} and 5%Er^{3+}, respectively). We do not observe any emission from the $^4I_{9/2}$ state of Er^{3+}, which would be located at about 12 450 cm^{-1}, corresponding to NIR photons around 805 nm [22,28]. Because the energy difference of the $^4I_{9/2}$ state to the next lower-lying $^4I_{11/2}$ state is about 2200 cm^{-1}, the gap can be bridged by only three phonons in YVO_4. For a three-phonon process, nonradiative multiphonon relaxation is much faster than that of radiative decay (emission) and this explains the absence of the $^4I_{9/2}$ emission in YVO_4.

Reports on three-photon splitting in the literature are based on room-temperature measurements, and therefore, we perform room-temperature luminescence and luminescence decay measurements to allow for comparison with the literature. However, to further investigate the possibility of (weak) emission from the $^4I_{9/2}$ level, also low-temperature (4 and 50 K) emission measurements are performed for samples of YVO_4:0.5%Er^{3+} and YVO_4:2%Er^{3+} under excitation of 522 nm [Figs. 2(c) and 2(d)]. At low temperatures, multiphonon relaxation will slow down and possibly allow for the observation of weak $^4I_{9/2}$ emission at 4 K. The 0.5%Er^{3+} doping level will hamper efficient CR, and above 2%Er^{3+} efficient cross-relaxation from the $^4S_{3/2}$ level is expected to populate the $^4I_{9/2}$ state and possibly give rise to $^4I_{9/2}$ emission. However, none of the samples give out any detectable NIR emission around 805 nm, indicating that multiphonon quenching is strong for Er^{3+} in the vanadate host.

For energy transfer within the Er^3-Er^{3+} pair by electric dipole-dipole interaction (the most common mechanism

for energy transfer between lanthanide ions), the transfer probability is proportional to R_{Er-Er}^{-6} (where R_{Er-Er} is the distance between Er^{3+} neighbors) [29]. This means that with increasing Er^{3+} concentration in YVO_4 the interionic distances of Er^{3+}-to-Er^{3+} become smaller; this will promote the occurrence of CR processes between Er^{3+} ions, such as CR1, leading to a marked decrease of the emission from the $^4S_{3/2}$ state once the Er^{3+}-doping concentration exceeds 2% [Fig. 2(b)]. The CR1 process $^2H_{11/2},^4S_{3/2} + {}^4I_{15/2} \rightarrow {}^4I_{9/2} + {}^4I_{13/2}$ has an energy mismatch of about 700 cm^{-1}, starting from the $^4S_{3/2}$ level and is close to resonant starting from the $^2H_{11/2}$ level. The 700 cm^{-1} mismatch can be readily bridged by absorbing one phonon in YVO_4. The probability for energy transfer via dipole-dipole interaction also scales with the oscillator strengths of the transitions involved. A good estimate of the oscillator strengths can be obtained using Judd-Ofelt theory. The transition dipole moments (oscillator strengths) scale with $\sum_{\lambda=2,4,6} \Omega_\lambda U_\lambda^2$, where the reduced matrix elements, U_λ are fixed for transitions between energy levels of lanthanides and the Judd-Ofelt parameters, Ω_λ depend on the local surroundings of the lanthanide in the host lattice. Even without knowing the Judd-Ofelt parameters Ω_λ it can be predicted that transitions with large U_λ^2 values will give rise to stronger forced electric dipole transitions. For the $^4S_{3/2} \rightarrow {}^4I_{9/2}$ and $^2H_{11/2} \rightarrow {}^4I_{9/2}$ "donor" transitions, the reduced matrix elements U_λ^2 are large (0, 0.0729, 0.2560 for $\lambda = 2, 4, 6$) and (0.195, 0.065, 0.284), respectively [30]. Also, the Er^{3+} "acceptor" transition in the CR1 process ($^4I_{15/2} \rightarrow {}^4I_{13/2}$ transition) has large U_λ^2 values (0.0188, 0.1176, 1.4617). Therefore, the CR1 energy-transfer rate is expected to be high.

The situation for the CR2 energy-transfer process of $^4I_{9/2} + {}^4I_{15/2} \rightarrow {}^4I_{13/2} + {}^4I_{13/2}$ is different. Also, for CR2, there is an energy mismatch that is slightly larger (about 800 cm^{-1}) and requires an anti-Stokes process involving absorbing one phonon in YVO_4. Contrary to the situation for the $^4S_{3/2}$ level, which has the $^2H_{11/2}$ level at about 700 cm^{-1} higher energies, there is no higher energy level that can be thermally populated to allow for resonant energy transfer and the transfer relies on coupling with weaker vibronic transitions. Also, the reduced matrix elements U_λ^2 for the "donor" transition on Er^{3+} ($^4I_{9/2} \rightarrow {}^4I_{13/2}$) are smaller (0.0003, 0.0081, 0.64) [30]. In addition, fast multiphonon relaxation from the $^4I_{9/2}$ level to the $^4I_{11/2}$ level by three-phonon relaxation competes with the CR2 energy-transfer process. Evidence that the anti-Stokes CR2 energy transfer is not efficient is obtained from the trends shown in Fig. 2(b): the monotonic enhancement of 1000 nm emission intensity upon raising the Er^{3+} concentration indicates that, following the CR1 process, the resulting population in the $^4I_{9/2}$ state relaxes to the $^4I_{11/2}$ state, resulting in 1000 nm emission. In the case of an efficient CR2 process, the $^4I_{9/2}$ state would be depleted to populate the $^4I_{13/2}$ state directly, but not the $^4I_{11/2}$ state

of Er^{3+}, which would suppress the emission intensity of $^4I_{11/2} \rightarrow {}^4I_{15/2}$ around 1000 nm.

Additional evidence for the inefficiency of the CR2 process is obtained from emission spectra under direct excitation in the $^4I_{9/2}$ level at 805 nm [see Fig. S3(a) within the Supplemental Material [8]]. The ratio of the 1530–1000 nm emission ($I_{1530\,nm}/I_{1000\,nm}$) is measured for different Er^{3+} concentrations [see Fig. S3(b) within the Supplemental Material [8]]. If CR2 is efficient, the ratio should increase with increasing Er^{3+} concentrations, as the CR2 step between Er^{3+} neighbors ($^4I_{9/2} + {}^4I_{15/2}$) would result in two Er^{3+} ions in the $^4I_{13/2}$ state, both emitting at 1530 nm, and thus, enhancing the 1530 nm emission at the expense of the 1000 nm emission following $^4I_{9/2} \rightarrow {}^4I_{11/2}$ relaxation. On the contrary, if $^4I_{9/2}$ to $^4I_{11/2}$ multiphonon relaxation dominates, the ratio is expected to be constant and determined by $^4I_{9/2} \rightarrow {}^4I_{11/2} \rightarrow {}^4I_{13/2}$ relaxation processes. The results in Fig. S3(b) within the Supplemental Material [8] clearly show a constant ratio of about 50 between 0.5% and 5% Er^{3+}, the concentration regime in which cross-relaxation becomes efficient. For higher Er^{3+} concentration, the ratio even decreases (rather than increases), which can be explained by concentration quenching that affects the 1530 nm emission more than the 1000 nm emission, as confirmed by concentration-dependent emission decay measurements (see below).

Further information on the efficiency and processes involved in cross-relaxation between Er^{3+} neighbors at higher Er^{3+} concentrations can be obtained from luminescence decay curves. Figures 3(a)–3(c) show the decay curves of 856, 1000, and 1530 nm emissions, respectively, for YVO$_4$:x%Er^{3+} ($x = 0.25, 0.5, 1, 2, 3, 5, 10, 20$) samples under pulsed-light excitation of 522 nm. Up to an Er^{3+} concentration of 2%, the 856 nm emission shows a nearly identical decay behavior that is independent of concentration [Fig. 3(a)]. The decay behavior can be fitted to a single-exponential function, $I = A_0 \exp(-t/\tau_0)$ (I is luminescence intensity, A_0 is a constant, τ_0 is the lifetime for the single-exponential decay curve) with τ_0 around 11 μs. Once the Er^{3+} concentration exceeds 2%, the decay becomes faster and the average decay time, τ_{avg}, reduces to 3.7 μs at 20%Er^{3+}. The decay curves become nonexponential above 5%Er^{3+} and can be fitted by a biexponential function (see Table SI within the Supplemental Material [8]), $I = A_1 \exp(-t/\tau_1) + A_2 \exp(-t/\tau_2)$ (A_1 and A_2 are constants, τ_1 and τ_2 are the fast and slow lifetimes, respectively, of exponential components for the nonexponential decay curve). A more careful analysis of the concentration-dependent decay curves to extract cross-relaxation rates would involve an analysis using the shell model described in Refs. [31,32] and is beyond the scope of this paper. The fastening of the $^4S_{3/2}$ and $^2H_{11/2}$ emission decay is consistent with the decrease in emission intensity from these levels above doping concentrations of 2%Er^{3+} in Fig. 2(b), which confirms the occurrence of efficient CR energy transfer between Er^{3+} neighbors [Fig. 3(d)].
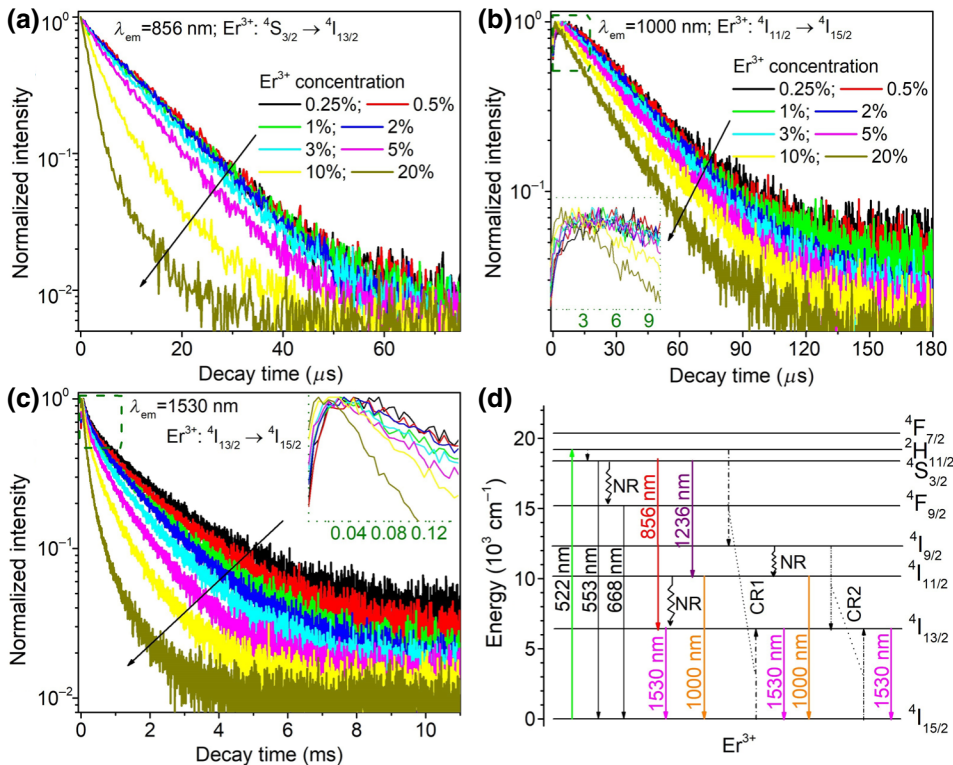

FIG. 3. (a)–(c) Luminescence decay curves of 856 (a), 1000 (b), and 1530 nm (c) for YVO$_4$:x%Er^{3+} ($x = 0.25, 0.5, 1, 2, 3, 5, 10, 20$) phosphors. Insets of (b),(c) show the rise times at short time intervals. (d) Energy-level diagram of Er^{3+} ($4f^{11}$), illustrating the energy-transfer mechanisms of photon splitting by multistep CR processes. For three-photon splitting, two consecutive cross-relaxation processes (CR1 and CR2) are required to occur with high efficiency.

In contrast, the decay curves of the 1000 nm emission do not change markedly up to Er^{3+} concentrations as high as 10% [Fig. 3(b)], with luminescence lifetimes of around 30 μs (see Table SI in Supplemental Material [8]). No cross-relaxation pathways with Er^{3+} neighbors are available for the $^4I_{11/2}$ state and only concentration quenching (energy migration to quenching centers) at high Er^{3+} concentration around 20% gives rise to quenching and explains shortening of the luminescence decay time. The rise time of the 1000 nm emission decay curves [inset of Fig. 3(b)] is around 5 μs, which indicates that the $^4I_{11/2}$ state of Er^{3+} is mainly fed by nonradiative relaxation (NR) from the upper $^4I_{9/2}$ state following CR1 energy transfer. The decay curves of the 1530 nm emission are shown in Fig. 3(c) and show long ms decay, which is typical for the $^4I_{13/2}$ emission of Er^{3+}. The lifetime decreases for increasing Er^{3+} concentrations, which is explained by energy transfer and energy migration to impurities and defects (acting as luminescence quenching centers). Energy migration becomes more pronounced in heavily doped samples. Due to feeding of the $^4I_{13/2}$ level by energy transfer (CR1) from $^2H_{11/2}$ or $^4S_{3/2}$ to $^4I_{13/2}$ states, a build-up in the initial tens of μs is observed in the 1530 nm decay curve [the inset of Fig. 3(c)], which, accelerated by faster CR1 energy transfer between Er^{3+} [3,21,23], becomes shorter at higher Er^{3+} concentration. In earlier work on triple quantum splitting for Er^{3+}, it was predicted by Miritello *et al.* that the anti-Stokes CR2 process occurred at 100%Er^{3+} to realize the triply splitting emission [23]. It is clear that, even if CR2 becomes more efficient at high doping concentrations, the corresponding 1530 nm emission will be strongly quenched by concentration quenching.

Based on the observations above, it is concluded that the CR1 process becomes efficient at Er^{3+} concentrations above 2% (leading to two-photon emission), but that the CR2 process required for triple-photon splitting does not occur efficiently. To further determine if and how efficiently the down-conversion for 1530 nm takes place from the $^2H_{11/2}$ and $^4S_{3/2}$ states through the double-splitting processes, we measure the relative intensities of the 654 ($^4F_{9/2}$ level) and 522 nm excitation peaks ($^2H_{11/2}$ level) for the

1000 and 1530 nm emissions at different Er^{3+} concentrations (1, 5, and 20% Er^{3+}). In the case of multiple-photon splitting, the ratio of the integral intensity of the green excitation band (approximately 522 nm) over that of the red excitation band (approximately 654 nm) by monitoring the emission wavelength at 1530 nm ($I_{1530\,nm}$) should be much greater than that by monitoring the emission at 1000 nm ($I_{1000\,nm}$): cross-relaxation from the excited $^2H_{11/2}$ and $^4S_{3/2}$ states at higher Er^{3+} concentrations will promote emission of more than one 1530 nm photon, but excitation in the $^4F_{9/2}$ state cannot, while a single 1000 nm photon follows excitation in both the $^2H_{11/2}, ^4S_{3/2}$ and $^4F_{9/2}$ states, as depicted in Fig. 3(d). The results are shown in Fig. 4. For YVO$_4$:1%Er^{3+}, the normalized excitation spectra indicate that the green excitation band while monitoring the 1530 nm emission is slightly stronger than that while monitoring the 1000 nm emission [Fig. 4(a)], and the ratio of $I_{1530\,nm}/I_{1000\,nm}$ is about 1.03 [Fig. 4(b)]. This observation reveals that the photon-splitting process for 1530 nm does not occur efficiently from the $^2H_{11/2}$ and $^4S_{3/2}$ states at Er^{3+}-doping concentrations around 1%, which is consistent with the lifetime measurements in Fig. 2(a). With increasing Er^{3+} concentration to 5%, and further to 20%, the normalized excitation spectra all feature a strong increment of the green excitation band under monitoring at 1530 nm over the red band under monitoring at 1000 nm [Fig. 4(a)], and the value of $I_{1530\,nm}/I_{1000\,nm}$ increases to 1.71 and 1.91 [Fig. 4(b)], respectively. These results validate that photon splitting for 1530 nm does occur from the $^2H_{11/2}$ and $^4S_{3/2}$ states and its efficiency strongly increases with increasing Er^{3+} content, to around 190% at about 20%Er^{3+}. At these high Er^{3+} concentrations, there is, however, considerable concentration quenching, which is evident from a shortening of the decay times for the $^4I_{11/2}$ and $^4I_{13/2}$ emissions and lowers the actual efficiency. The highest overall quantum yields will thus be realized in about 5%Er^{3+}-doped material, where the photon-splitting efficiency is around 70% and concentration quenching is still limited. Based on these observations, the upper limit for the overall quantum yield in YVO$_4$:Er^{3+} can be estimated to be about 170%.

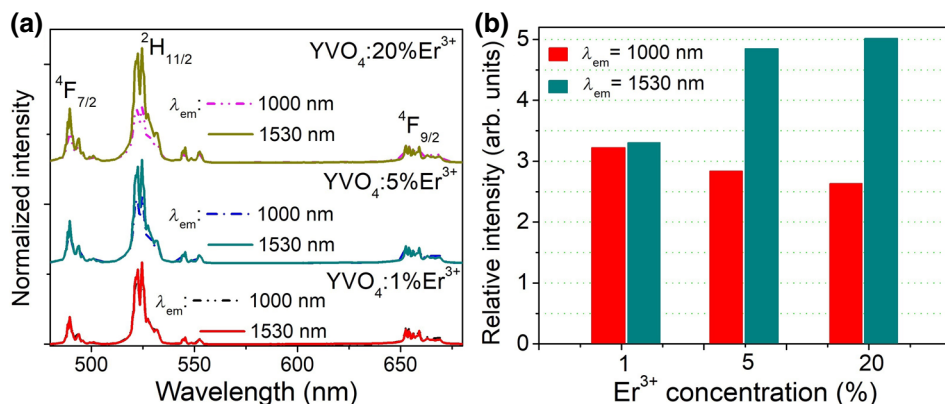FIG. 4. (a) Excitation spectra normalized at 654 nm (excitation into the $^4F_{9/2}$ excited state) of YVO$_4$:x%Er^{3+} ($x = 1, 5, 20$) phosphors, while monitoring 1000 (broken lines) or 1530 nm (solid lines) emissions. (b) The excitation intensities around 522 nm (into the $^2H_{11/2}, ^4S_{3/2}$ excited state) relative to the 654 nm excitation intensity, while monitoring the 1000 (red bars) or 1530 nm (green bars) emissions.

IV. OPTIMIZATION OF Er^{3+} THREE-PHOTON NIR QS

The main reason for the lack of three-photon NIR quantum splitting is the low efficiency of the CR2 step. The need for phonon assistance for CR2 transfer because of the energy mismatch of about 700–800 cm^{-1} means that the CR2 rate cannot compete with fast nonradiative multiphonon relaxation from the $^4I_{9/2}$ level, involving emission of three vanadate vibrations to bridge the about 2200 cm^{-1} energy gap between the $^4I_{9/2}$ and $^4I_{11/2}$ levels. The multiphonon relaxation rate can be significantly lowered by reducing the energy of the vibrations (phonons) by choosing a low-phonon energy host. Radiative transition rates (W_R) for excited $4f$ levels of RE^{3+} activators are typically 10^2–10^4 s^{-1} [33] [shaded area in Fig. 5(a)]. The NR rate (W_{NR}) for a fixed ΔE is determined by the maximum phonon energy in the host. Modeling of multiphonon relaxation was pioneered by Riseberg and Moos [34], and

resulted in the well-known energy-gap law describing the multiphonon relaxation rate at 0 K:

$$W_{NR} = C \exp(-\alpha \Delta E), \qquad (1)$$

where C and α are positive constants related to the host. The semilog$_{10}$ graph in Fig. 5(a) depicts the experimentally determined W_{NR} value versus ΔE in some classical hosts [30,34–39].

Based on the energy gap law, it is found that, for the $^4I_{9/2} \rightarrow {}^4I_{11/2}$ transition on Er^{3+} with $\Delta E \sim 2200$ cm^{-1}, the W_{NR} of the $^4I_{9/2}$ excited state becomes similar to or slower than that of W_R in hosts with low phonon energies, such as fluorides, chlorides, and bromides, so that five or more phonons are needed to bridge the gap. In the YVO$_4$ host, the W_{NR} of the Er^{3+} $^4I_{9/2}$ state is at least 100 times higher than that of the W_R and no emission is detected from the $^4I_{9/2}$ state. The semilog$_{10}$ graph in Fig. 5(b) further shows the dependence of W_{NR}/W_R ratio of the Er^{3+} $^4I_{9/2}$ energy level as a function of phonon energy in some classical hosts [30,40–43]. In hosts with high phonon energies, the W_{NR}/W_R ratio dramatically increases, while in fluorides, with a smaller phonon energy of 350–450 cm^{-1}, the W_{NR}/W_R ratio is around 10–100, which is consistent with the observation of weak $^4I_{9/2}$ emission in fluorides [30]. A strong reduction of W_{NR} for the Er^{3+} $^4I_{9/2}$ energy level is crucial to realize efficient triple splitting into three 1530 nm photons. A possible host is chalcogenide glasses, with a lower phonon energy of about 250 cm^{-1} [44–47], where the W_{NR}/W_R ratio of the Er^{3+} $^4I_{9/2}$ state is predicted to be about one [1.0 in Ref. [45], 0.74 in Ref. [46], and 0.57 in Ref. [47]; green stars in Fig. 5(b)]. This is consistent with the observation of an intense $^4I_{9/2}$ emission for Er^{3+} at room temperature, demonstrating that the radiative and nonradiative multiphonon relaxation rates are similar [44–48].

For triple-photon splitting, the CR2 energy-transfer process has to compete with radiative and nonradiative decay. As discussed above, in a low-phonon host (like chalcogenide glasses), the nonradiative decay rate can be reduced. Still, it will be challenging to realize a CR2 transfer rate that is faster than that of radiative and nonradiative decay from the $^4I_{9/2}$ level because of the energy mismatch of about 700–800 cm^{-1}. Phonon absorption is needed to make up for the energy difference between the $^4I_{9/2}$ energy (approximately 12 600 cm^{-1}) and two times the $^4I_{13/2}$ energy ($2\times \sim 6700$ cm$^{-1} = 13\,400$ cm^{-1}). In a chalcogenide glass (or similar low-phonon host), this means that three phonons of about 250 cm^{-1} have to be absorbed to make up this energy mismatch. The temperature dependence of phonon (absorption) assisted processes is given as [36,49]
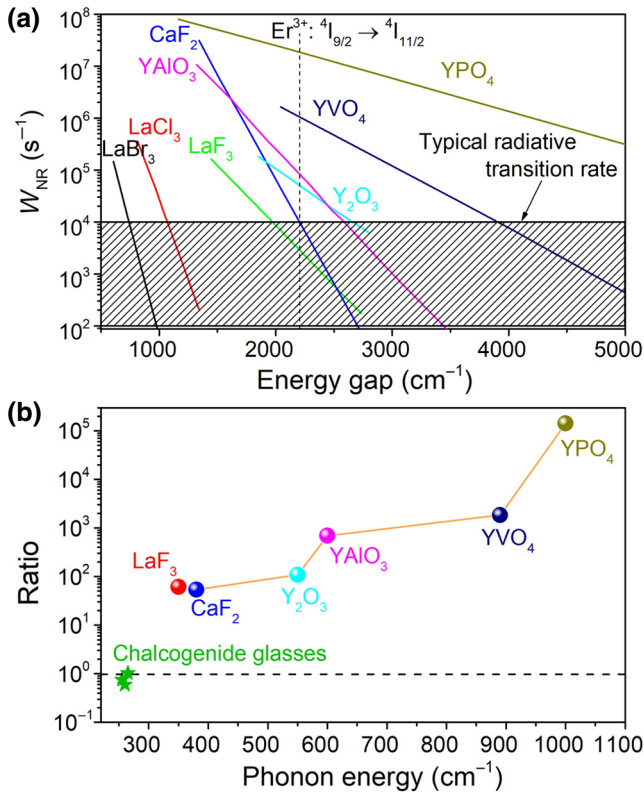
$$W_a(T) = W_a(T=0)n^{N_a}, \qquad (2)$$

FIG. 5. (a) Dependence of multiphonon relaxation rate on energy gap for lanthanide ions in various hosts (data from Refs. [30,34–39]). Shaded area shows the range of typical radiative transition rates for parity-forbidden f-f transitions in lanthanides. (b) Ratio of nonradiative multiphonon relaxation rate to that of radiative decay rate for the $^4I_{9/2} \rightarrow {}^4I_{11/2}$ (approximately 2200 cm^{-1}) transition in various hosts, as expected based on the energy-gap law. Green stars give experimentally observed ratios for the $^4I_{9/2}$ level of Er^{3+} in a variety of low-phonon chalcogenide glasses (data from Refs. [44–46]).

where N_a is the number of phonons absorbed ($\Delta E/\hbar\omega$) to bridge the energy mismatch, ΔE, for a multiphonon-assisted process; n is the phonon occupation number [36,50],

$$n = (e^{[\hbar\omega/kT]} - 1)^{-1}. \tag{3}$$

In a chalcogenide glass, a three-phonon-assisted process involving simultaneous absorption of three about 250 cm^{-1} phonons is required for CR2. By fitting to Eq. (2), this gives a factor of 0.06 for n^{N_a}, and thus, lowers the rate for the CR2 process, which already has a relatively low probability, as it involves a three-phonon-assisted energy-transfer process. Whether or not CR2 between nearest neighbors of Er^{3+} can be efficient in low-phonon hosts needs experimental verification, and it will be interesting to test if triple-photon splitting is feasible in chalcogenide hosts.

V. CONCLUSIONS

Photon splitting from the $^2H_{11/2}$,$^4S_{3/2}$ states levels of Er^{3+} is systematically studied in the YVO$_4$ host. The energy-level scheme of Er^{3+} allows for splitting one green photon into three 1530 nm NIR photons, as reported in the literature. To investigate the efficiency of the three-photon splitting process, a systematic study involving emission and excitation spectra, as well as luminescence decay curves, is conducted for a wide range of Er^{3+} doping concentrations. For Er^{3+} concentrations above 1%, a CR1 energy-transfer step ($^2H_{11/2}$,$^4S_{3/2}$ + $^4I_{15/2} \rightarrow$ $^4I_{9/2}$ + $^4I_{13/2}$) becomes efficient, resulting in double splitting of green photons into two NIR photons. A CR2 step ($^4I_{9/2}$ + $^4I_{15/2} \rightarrow$ $^4I_{13/2}$ + $^4I_{13/2}$) is crucial for triple-photon splitting and is demonstrated to be inefficient in YVO$_4$:Er^{3+} because of fast multiphonon relaxation from the $^4I_{9/2}$ level, which effectively competes with the slow anti-Stokes phonon-assisted CR2 process. By comparing the ratio of the green and red bands in the excitation spectra (monitoring emission at 1000 and 1530 nm, respectively), a maximum quantum efficiency is determined to be about 170% for YVO$_4$:5%Er^{3+}. At higher doping concentrations, the CR1 process reaches close to unity efficiency, which would allow for close to 200% quantum efficiencies, but concentration quenching lowers the actual efficiency. The three-photon process does not occur because of the inefficiency of the CR2 process.

To realize triple NIR photon splitting in Er^{3+}-doped hosts, it is crucial to suppress multiphonon relaxation from the $^4I_{9/2}$ level. This can be done in low-phonon hosts, such as chalcogenide glasses. Even then, the prospects are cumbersome because the CR2 process is an anti-Stokes energy-transfer process requiring three-phonon assistance in low-phonon host lattices, and it may not be possible to make CR2 faster than that of decay from the $^4I_{9/2}$ level, even for nearest Er^{3+} neighbors. The present insights

into the photon splitting of Er^{3+} clearly identify the possibilities and challenges in the development of efficient UV-vis-NIR downconvertors based on Er^{3+} and provide guidelines to realize higher photon-splitting efficiencies.

[1] B. van der Zwaan and A. Rabl, Prospects for PV: A learning curve analysis, Sol. Energy **74**, 19 (2003).

[2] W. Shockley and H. J. Queisser, Detailed balance limit of efficiency of *p*-*n* junction solar cells, J. Appl. Phys. **32**, 510 (1961).

[3] X. B. Chen, J. G. Wu, X. L. Xu, Y. Z. Zhang, N. Sawanobori, C. L. Zhang, Q. H. Pan, and G. J. Salamo, Three-photon infrared quantum cutting from single species of rare-earth Er^{3+} ions in Er$_{0.3}$Gd$_{0.7}$VO$_4$ crystalline, Opt. Lett. **34**, 887 (2009).

[4] B. S. Richards, Enhancing the performance of silicon solar cells via the application of passive luminescence conversion layers, Sol. Energy Mater. Sol. Cells **90**, 2329 (2006).

[5] B. M. van der Ende, L. Aarts, and A. Meijerink, Lanthanide ions as spectral converters for solar cells, Phys. Chem. Chem. Phys. **11**, 11081 (2009).

[6] Q. Y. Zhang and X. Y. Huang, Recent progress in quantum cutting phosphors, Prog. Mater. Sci. **55**, 353 (2010).

[7] T. Trupke, M. A. Green, and P. Würfel, Improving solar cell efficiencies by down-conversion of high-energy photons, J. Appl. Phys. **92**, 1668 (2002).

[8] See the Supplemental Material at http://link.aps.org/supplemental/10.1103/PhysRevApplied.13.024076 for the efficiency gain enabled by an ideal downconversion layer for a solar cell ($E_g \sim 0.8$ eV), emission and excitation spectra of YVO$_4$:1%Er^{3+}; near-infrared emission properties for YVO$_4$:*x*%Er^{3+} for 805 nm excitation (OPO laser); and calculated decay times of Er^{3+} emissions around 856, 1000, and 1530 nm for YVO$_4$:*x*%Er^{3+}.

[9] P. Vergeer, T. J. H. Vlugt, M. H. F. Kox, M. I. Den Hertog, J. P. J. M. van der Eerden, and A. Meijerink, Quantum cutting by cooperative energy transfer in Yb$_x$Y$_{1-x}$PO$_4$:Tb^{3+}, Phys. Rev. B **71**, 014119 (2005).

[10] Q. Y. Zhang, C. H. Yang, and Y. X. Pan, Cooperative downconversion in GdAl$_3$(BO$_3$)$_4$:RE^{3+}, Yb^{3+} (RE = Pr, Tb, and Tm), Appl. Phys. Lett. **90**, 021107 (2007).

[11] D. Q. Chen, Y. S. Wang, Y. L. Yu, P. Huang, and F. Y. Weng, Near-infrared quantum cutting in transparent nanostructured glass ceramics, Opt. Lett. **33**, 1884 (2008).

[12] B. M. van der Ende, L. Aarts, and A. Meijerink, Near-infrared quantum cutting for photovoltaics, Adv. Mater. **21**, 3073 (2009).

[13] J. J. Eilers, D. Biner, J. T. Van Wijngaaerden, K. Krämer, H.-U. Güdel, and A. Meijerink, Efficient visible to infrared quantum cutting through downconversion with the Er^{3+}-Yb^{3+} couple in Cs$_3$Y$_2$Br$_9$, Appl.Phys. Lett. **96**, 151106 (2010).

[14] T. Yu, D. C. Yu, H. H. Li, and Q. Y. Zhang, Single-band near-infrared quantum cutting of Ho^{3+}-Yb^{3+} codoped KLu$_2$F$_7$ phosphors by energy clustering, J. Alloys Compd. **695**, 1154 (2017).

[15] K. M. Deng, T. Gong, L. X. Hu, X. T. Wei, Y. H. Chen, and M. Yin, Efficient near-infrared quantum cutting in NaYF$_4$: Ho^{3+}, Yb^{3+} for solar photovoltaics, Opt. Express **19**, 1749 (2011).

[16] D. C. Yu, X. Y. Huang, S. Ye, M. Y. Peng, Q. Y. Zhang, and L. Wondraczek, Three-photon near-infrared quantum splitting in β-NaYF$_4$:Ho^{3+}, Appl. Phys. Lett. **99**, 161904 (2011).

[17] X. B. Chen, S. Li, G. J. Salamo, Y. L. Li, L. Z. He, G. J. Yang, Y. Gao, and Q. L. Liu, Sensitized intense near-infrared downconversion quantum cutting three-photon luminescence phenomena of the Tm^{3+} ion activator in Tm^{3+}Bi^{3+}:YNbO$_4$ powder phosphor, Opt. Express **23**, A51 (2015).

[18] D.-C. Yu, R. Martín-Rodríguez, Q. Y. Zhang, A. Meijerink, and F. T. Rabouw, Multi-photon quantum cutting in Gd$_2$O$_2$S:Tm^{3+} to enhance the photo-response of solar cells, Light: Sci. Appl. **4**, e344 (2015).

[19] L. L. Huang, L. Lin, B. Zheng, H. Huang, Z. H. Feng, Z. Z. Wang, X. Y. Li, and Z. Q. Zheng, Simultaneous excitation and emission enhancement of near-infrared quantum cutting in β-NaYF$_4$:Er nanoparticles by double plasmon modes of noble metals, Opt. Commun. **441**, 170 (2019).

[20] J. J. Zhou, Y. Teng, X. F. Liu, S. Ye, Z. J. Ma, and J. R. Qiu, Broadband spectral modification from visible light to near-infrared radiation using Ce^{3+}-Er^{3+} codoped yttrium aluminium garne, Phys. Chem. Chem. Phys. **12**, 13759 (2010).

[21] X. B. Chen, S. Li, K. Z. Wang, Z. L. Wu, G. Y. Zhao, J. F. Tao, H. Ma, W. Lin, H. L. Liu, L. L. Hu, P. Guo, and G. J. Salamo, Two-photon, three-photon, and four-photon near-infrared quantum cutting luminescence of an Er^{3+} activator in tellurium glass phosphor, Appl. Opt. **55**, 3343 (2016).

[22] P. Kabro, J. A. Capobianco, F. S. Ermeneux, R. Moncorgé, M. Bettinelli, and E. Cavalli, Excited state dynamics and energy transfer processes in YVO$_4$:Er^{3+} crystals, J. Appl. Phys. **82**, 3983 (1997).

[23] M. Miritello, R. L. Savio, P. Cardile, and F. Priolo, Enhanced down conversion of photons emitted by photoexcited Er$_x$Y$_{2-x}$Si$_2$O$_7$ films grown on silicon, Phys. Rev. B **81**, 041411 (2010).

[24] F. J. Manjón, P. Rodríguez-Hernández, A. Munñoz, A. H. Romero, D. Errandonea, and K. Syassen, Lattice dynamics of YVO$_4$ at high pressures, Phys. Rev. B **81**, 075202 (2010).

[25] N. Rakov and G. S. Maciel, Near-infrared quantum cutting in Ce^{3+}, Er^{3+}, and Yb^{3+} doped yttrium silicate powders prepared by combustion synthesis, J. Appl. Phys. **110**, 083519 (2011).

[26] R. D. Shannon, Revised effective ionic radii and systematic studies of interatomic distances in halides and chalcogenides, Acta Cryst. **A32**, 751 (1976).

[27] V. D. Rodíguez, V. K. Tikhomirov, J. Méndez-Ramos, A. C. Yanes, and V. V. Moshchalkov, Towards broad range and highly efficient down-conversion of solar spectrum by Er^{3+}-Yb^{3+} co-doped nano-structured glass-ceramics, Sol. Energy Mater. Sol. Cells **94**, 1612 (2010).

[28] L. Gomes, A. F. H. Librantz, F. H. Jagosick, W. A. L. Alves, I. M. Ranieri, and S. L. Baldochi, Energy transfer rates and population inversion of ^{4}I$_{11/2}$ excited state of Er^{3+} investigated by means of numerical solutions of the rate equations system in Er:LiYF$_4$ crystal, J. Appl. Phys. **106**, 103508 (2009).

[29] D. L. Dexter, A theory of sensitized luminescence in solids, J. Chem. Phys. **21**, 836 (1953).

[30] M. J. Weber, Probabilities for radiative and nonradiative decay of Er^{3+} in LaF$_3$, Phys. Rev. **157**, 262 (1967).

[31] S. O. Vasquez and C. D. Flint, A shell model for cross relaxation in elpasolite crystals: Application to the ^{3}P$_0$ and ^{1}G$_4$ states of Cs$_2$NaY$_{1-x}$Pr$_x$Cl$_6$, Chem. Phys. Lett. **238**, 378 (1995).

[32] M. Campbell and C. D. Flint, Back transfer in the ^{4}S$_{3/2}$ state of Cs$_2$NaEr$_x$Y$_{1-x}$Cl$_6$. extension of the shell model, Spectrochim. Acta **A54**, 1583 (1998).

[33] K. Soga, W. Z. Wang, R. E. Riman, J. B. Brown, and K. R. Mikeska, Luminescent properties of nanostructured Dy^{3+}- and Tm^{3+}-doped lanthanum chloride prepared by reactive atmosphere processing of sol-gel derived lanthanum hydroxide, J. Appl. Phys. **93**, 2946 (2003).

[34] L. A. Riseberg and H. W. Moos, Multiphonon orbit-lattice relaxation of excited states of rare-earth ions in crystals, Phys. Rev. **174**, 429 (1968).

[35] L. A. Riseberg and H. W. Moos, Multiphonon Orbit-Lattice Relaxation in LaBr$_3$, LaCl$_3$, and LaF$_3$, Phys. Rev. Lett. **19**, 1423 (1967).

[36] M. P. Miller and J. C. Wright, Multiphonon and energy transfer relaxation in charge compensated crystlas, J. Chem. Phys. **71**, 324 (1979).

[37] M. J. Weber, Multiphonon relaxation of rare-earth ions in yttrium orthoaluminate, Phys. Rev. B **8**, 54 (1973).

[38] F. S. Ermeneux, C. Goutaudier, R. Moncorgé, Y. Sun, R. L. Cone, E. Zannoni, E. Cavalli, and M. Bettinelli, Multiphonon relaxation in YVO$_4$ single crystals, Phys. Rev. B **61**, 3915 (2000).

[39] H. Zheng and R. S. Meltzer, Relaxation of rare-earth ions in YPO$_4$ crystal, J. Lumin. **122–123**, 478 (2007).

[40] J. A. Capobianco, P. Kabro, F. S. Ermeneux, R. Moncorgé, M. Bettinelli, and E. Cavalli, Optical spectroscopy, fluorescence dynamics and crystal-field analysis of Er^{3+} in YVO$_4$, Chem. Phys. **214**, 329 (1997).

[41] G. A. Kumar, R. Riman, S. C. Chae, Y. N. Jang, I. K. Bae, and H. S. Moon, Synthesis and spectroscopic characterization of CaF$_2$:Er^{3+} single crystal for highly efficient 1.53 μm amplification, J. Appl. Phys. **95**, 3243 (2004).

[42] C. A. Morrison, R. P. Leavitt, J. B. Gruber, and N. C. Chang, Optical spectra, energy levels, and crystal-field analysis of tripositive rare-earth ions in Y_2O_3. III. Intensities and g values for C_2 sites, J. Chem. Phys. **79,** 4758 (1983).

[43] D. K. Sardar, S. Chandrasekharan, K. L. Nash, and J. B. Gruber, Optical intensity analyses of Er^{3+}:$YAlO_3$, J. Appl. Phys. **104,** 023102 (2008).

[44] D. K. Sardar, J. B. Gruber, B. Zandi, J. A. Hutchinson, and C. W. Trussell, Judd-Ofelt analysis of the Er^{3+}($4f^{11}$) absorption intensities in phosphate glass: Er^{3+}, Yb^{3+}, J. Appl. Phys. **92,** 2041 (2003).

[45] C. C. Ye, D. W. Hewak, M. Hempstead, B. N. Samson, and D. N. Payne, Spectral properties of Er^{3+}-doped gallium lanthanum sulphide glass, J. Non-Cryst. Solids **208,** 56 (1996).

[46] R. S. Quimby and B. G. Aitken, Multiphonon energy gap law in rare-earth doped chalcogenide glass, J. Non-Cryst. Solids **320,** 100 (2003).

[47] V. Moizan, V. Nazabal, J. Troles, P. Houizot, J.-L. Adam, J.-L. Doualan, R. Moncorgé, F. Smektala, G. Gadret, S. Pitois, and G. Canat, Er^{3+}-doped GeGaSbS glasses for mid-IR fibre laser application: Synthesis and rare earth spectroscopy, Opt. Mater. **31,** 39 (2008).

[48] R. Reisfeld, in *Radiationless Processes*, edited by B. DiBartolo (Plenum Press, New York, 1980), pp. 489.

[49] F. Auzel, Multiphonon-assisted anti-stokes and stokes fluorescence of triply ionnized rare-earth ions, Phys. Rev. B **13,** 2809 (1976).

[50] D. C. Yu, J. Ballato, and R. E. Riman, Temperature-dependence of multiphonon relaxation of rare-earth ions in solid-state hosts, J. Phys. Chem. C **120,** 9958 (2016).